ARCHIVE OF MECHANICAL ENGINEERING

VOL. LXV 2018 Number 2

DOI: 10.24425/123021

Key words: cohesive zone model, debonding, Finite Element Method

FERGYANTO E. GUNAWAN [1]

STATIC AND DYNAMIC DEBONDING STRENGTH OF BUNDLED GLASS FIBERS

Experimental design and computational model for predicting debonding initiation and propagation are of interest of scientists and engineers. The design and model are expected to explain the phenomenon for a wide range of loading rates. In this work, a method to measure and quantify debonding strength at various loading rates is proposed. The method is experimentally verified using data obtained from a static test and a pulse-type dynamic test. The proposed method involves the cohesive zone model, which can uniquely be characterized with a few parameters. Since those parameters are difficult to be measured directly, indirect inference is deployed where the parameters are inferred by minimizing discrepancy of mechanical response of a numerical model and that of the experiments. The main finding suggests that the design is easy to be used for the debonding characterization and the numerical model can accurately predict the debonding for the both loading cases. The cohesive strength of the stress-wave case is significantly higher than that of the static case; meanwhile, the cohesive energy is twice larger.

1. Introduction

Composite materials are extremely important in development of many recent technologies that require engineering materials having very high strength-to-weight ratio. For example, each Boeing 787 contains approximately 35 tons of carbon fiber reinforced plastic [1]. Traditionally, damages and failures in composite materials are harder to model in comparison with those in conventional materials. However, during the last few years, we have witnessed that the energy-based approach using the cohesive zone model seems to provide reasonable prediction particularly for delamination and debonding [2–5]. This numerical approach is more pervasive than the analytical approach [6].

[1] *Industrial Engineering Department, BINUS Graduate Program – Master of Industrial Engineering, Bina Nusantara University, Jakarta, Indonesia 11480 Email: fgunawan@binus.edu*

As for the debonding quantification, the existing methods can be categorized into the micro-bond method [7–10], the fiber pull-out method [11–14], the fiber push-out method [15–18], and the single-fiber fragmentation test [25–27]. However, each of those existing methods is often only suitable for a specific mode and rate of loading. The micro bond and fragmentation test methods are only suitable when the applied load is static. The push-out test method can be used for static and dynamic loads; however, a major adjustment has to be made particularly in the specimen design when the applied load is dynamic.

In [3], we proposed a method for debonding test at high loading rate. In the present work, the same method will be extended to the static case and the debonding behavior will be discussed for both loading conditions. This article should demonstrate that the proposed method is suitable to test the debonding phenomenon at any rates of loading.

2. Debonding experiment

2.1. Static and dynamic debonding specimens

The proposed specimen for the static and dynamic debonding tests is shown in Fig. 1. It has the following geometry: the specimen nominal diameter d = 9.5 mm, the diameter of the bundled fiber d_f = 1 mm and 2 mm, the notch depth c = 3 mm, and the gauge location b was 20 mm from the notch. For the static test, the specimen length L is 72 mm, and the notch is located in the middle. Meanwhile, for the dynamic test, the length is 200 mm, and the notch L_n is located at 90 mm. The fiber material has Young's modulus of 76 GPa, Poisson's ratio of 0.23, and density of 1165 kg/m^3. Meanwhile, the matrix material has Young's modulus of 5.4 GPa, Poisson's ratio of 0.32, and density of 2450 kg/m^3.

The specimens are fabricated in the laboratory. Glass fibers with 7 μm nominal diameter are bundled up into 1 mm and 2 mm diameters. The fiber bundle is placed

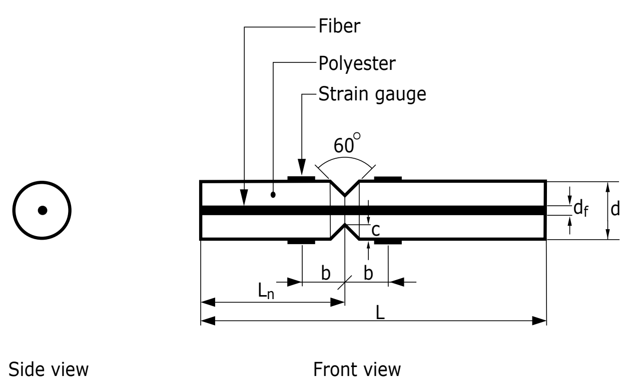

Fig. 1. Proposed specimen geometry for the static and dynamic debonding tests [3]

along the axis of a cylindrical mold. Then, the unsaturated polyester resin is poured into the mold with prudential attention to be free of air bubbles in the specimen. Subsequently, the specimen is cured at 75°C for two hours in an oven and cooled down in the oven. Finally, a v-notch is introduced to each specimen for a depth of 3 mm by using a lathe machine.

2.2. Experimental apparatus for static and dynamic debonding

In the static test, the specimen is placed in the holder depicted in Fig. 2, and then is pulled with a tension test machine until the debonding take places on the fiber-matrix interface. Three data are recorded: the applied load, the debonding length, and the specimen displacement.

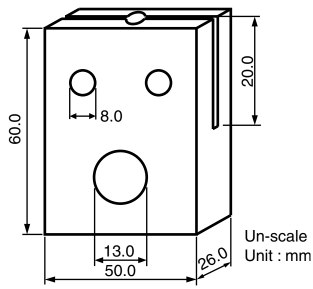

Fig. 2. Design and geometry of the holder for the static test

In the dynamic test, the debonding is generated using a Hopkinson bar test apparatus as shown in Fig. 3. In this test, the specimen is placed ahead of the load transfer rod, which is made of the steel material and has a size of 20 mm in diameter and 1 m in length. The projectile is a sphere made of steel material with a diameter

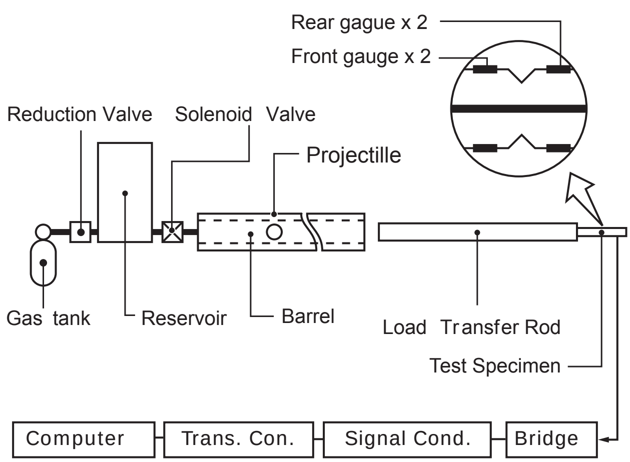

Fig. 3. Testing apparatus for the stress-pulse debonding test [3]

of 20 mm. Four strain gauges are mounted to the specimen, two gauges before the notch, and two gauges after. Those gauges are connected to a Wheatstone bridge, then to a transient converter, which sampling the data at every 0.1 μs.

From the both tests, the debonding on the specimens is visible with a naked eye (for an example, see Fig. 4); thus, the debonding length can be measured easily.

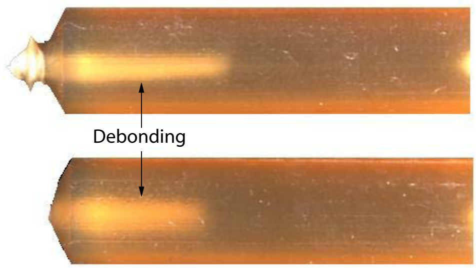

Fig. 4. The visible debonding on the fiber-matrix interface of the specimen [3]

2.3. Experimental results of static and dynamic tests

In the static test, the main results are the debonding length and its associated-applied load; meanwhile, the main results of the dynamic tests are the debonding length and its associated maximum strain of the reflected stress-wave at the rear of the notch. For the sake of conciseness, these results will be presented in Section 3.3 in conjunction with results of the numerical predictions.

3. Numerical analysis

Debonding is often difficult to be characterized directly from experimentally measured data. An indirect approach is more common and is adopted in this work. The approach is based on the finite element method with a cohesive zone model to model the decohesion. The parameters associated with the cohesive zone model are established iteratively such that the numerical model produced responses similar to those observed in the experiments in microscopic and macroscopic scales.

3.1. Debonding initiation and propagation model

We consider the interface as a surface with normal direction $\mathbf{n}$ and tangential direction $\mathbf{s}$. At any point on the surface, the traction $\mathbf{t}$ has two components, i.e., in the normal direction $t_\mathbf{n}$ and in the tangential direction $t_\mathbf{s}$; thus, $\mathbf{t} = (t_\mathbf{n}\ t_\mathbf{s})^T$, and the associated deformation: $\boldsymbol{\Delta} = (\Delta_\mathbf{n}\ \Delta_\mathbf{s})^T$. The traction $\mathbf{t}$ and deformation $\boldsymbol{\Delta}$ are related according to the bilinear softening model [19, 20] (see Fig. 5).

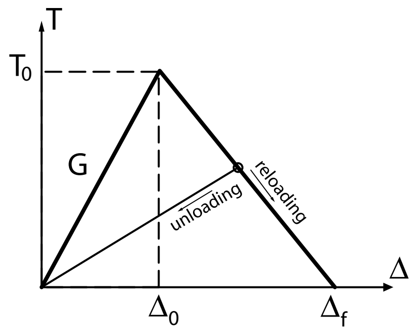

Fig. 5. The bilinear traction-separation model [3]

The debonding is started when

$$\left(\frac{\langle t_{\mathbf{n}}\rangle}{t_{\mathbf{n}}^{c}}\right)^{2}+\left(\frac{t_{\mathbf{s}}}{t_{\mathbf{s}}^{c}}\right)^{2}=1, \tag{1}$$

where $t_{\mathbf{n}}^{c}$ and $t_{\mathbf{s}}^{c}$ are the critical material strength in normal and in shear, respectively; $\langle\cdot\rangle$ is the Macaulay brackets, which set any negative value to zero. The debonding propagation is governed by [21]:

$$\left(\frac{G_{\mathbf{n}}}{G_{\mathbf{n}}^{c}}\right)+\left(\frac{G_{\mathbf{s}}}{G_{\mathbf{s}}^{c}}\right)=1, \tag{2}$$

where G denotes the strain energy, and $G_{\mathbf{n}}^{c}$ and $G_{\mathbf{s}}^{c}$ are the critical strain energy in normal and in shear, respectively.

3.2. The Finite Element models and fracture parameters

Numerical analysis is carried out using the finite element method by means of Abaqus finite element package [19].

For the static case, Abaqus/Standard is used with the finite element model mesh that is depicted in Fig. 6. The model is axisymmetrical. It has 1826 nodes and 1707 elements for 1 mm bundled-fiber diameter, and 1723 nodes and 1605 elements for 2 mm bundled-fiber diameter. Zero thickness interface elements are used along the matrix interface and the fiber-matrix interface (see Fig. 6). The model is subjected to uniform displacement at the right end and the displacement was increased to 0.5 mm in 100 steps. Thus, we assume that the matrix fracture and the debonding occurred along a line in the 2D model.

The fracture parameters – $t_{\mathbf{n}}^{c}, t_{\mathbf{s}}^{c}, G_{\mathbf{n}}^{c}, G_{\mathbf{s}}^{c}$ – for both matrix interface and fiber-matrix interface are determined iteratively in two steps such that the finite element model provides mechanical response similar to that observed in the experiment. The matrix interface parameters are determined in the first step, and the fiber-

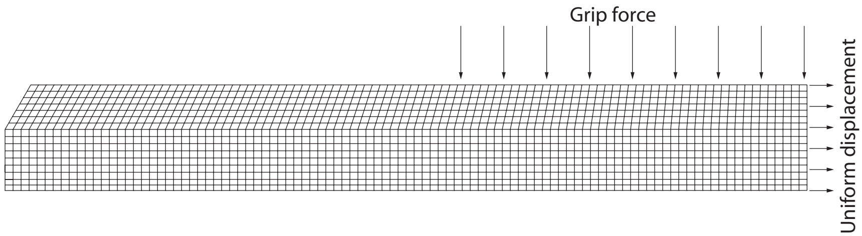

(a)

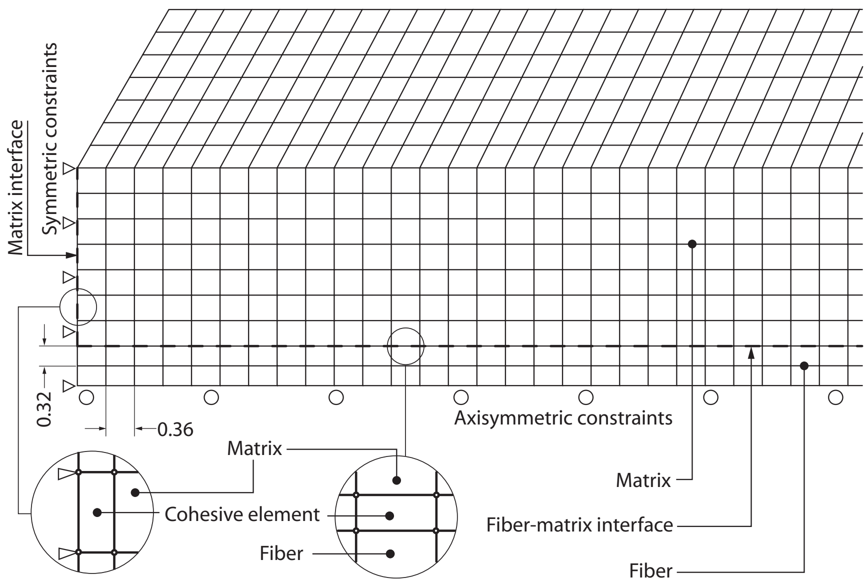

(b)

Fig. 6. Axisymmetrical FE model mesh for the static test specimen; (a) global scale, and (b) detailed scale

matrix interface parameters are in the second step. As results, the interface fracture parameters are obtained: $t_{\mathbf{n}}^{c} = 15$ MPa, $t_{\mathbf{s}}^{c} = 15$ MPa, $G_{\mathbf{n}}^{c} = 1.0$ MPa · mm, and $G_{\mathbf{s}}^{c} = 1.0$ MPa · mm.

Abaqus/Explicit is used for the dynamic case with the finite element mesh of Fig. 7. The mesh has 272 013 elements and 275 355 nodes with an element length about 6.25×10^{-2} mm. On the model left end, uniform pressure is applied and is varied in time following a half-sine function where peak and period are adjusted so that the strain time history at the 'gauge' points closely follows the specimen response. The interface fracture parameters are obtained in the same manner as for the static case. As results, the interface fracture parameters are obtained: $t_{\mathbf{n}}^{c} = 54$ MPa, $t_{\mathbf{s}}^{c} = 67$ MPa, $G_{\mathbf{n}}^{c} = 2.0$ MPa · mm, and $G_{\mathbf{s}}^{c} = 2.0$ MPa · mm.

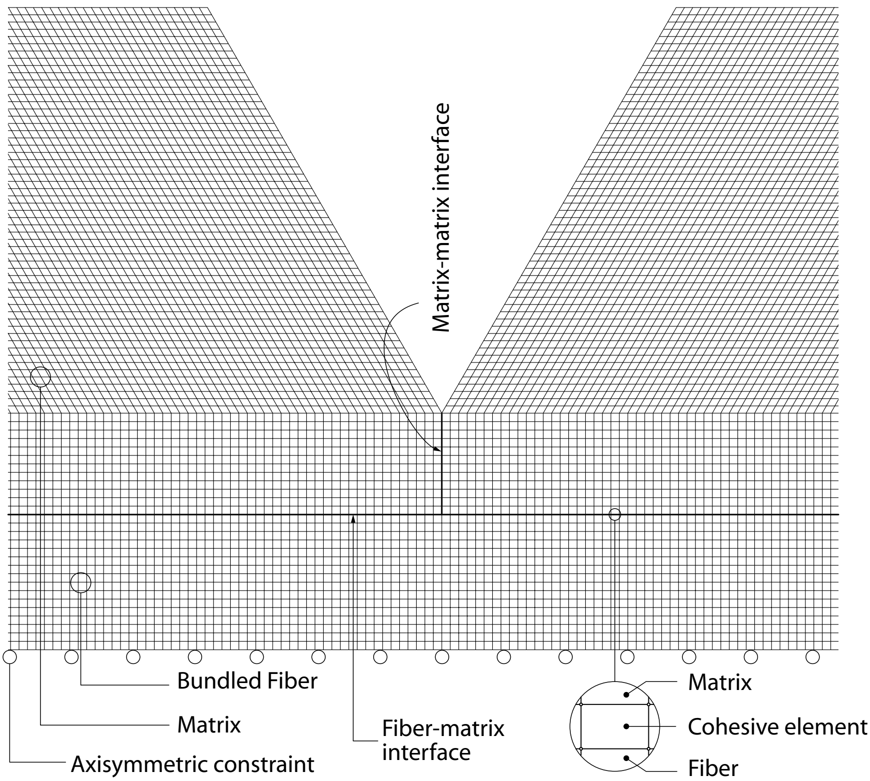

Fig. 7. Axisymmetrical FE model mesh for the dynamic test specimen in a detailed scale [3]

3.3. Discussion

As stated in Section 3, the parameters of the interface materials should be calibrated in such a way that the computational model provides mechanical responses in the macroscopic and microscopic scales that similar to those observed in the experiments. The calibration is made for the static case as well as for the dynamic case. For the static case, the similarity in the macroscopic scale is concluded by comparing the applied load-displacement curve obtained from the computational model to that recorded in the experiment. In the microscopic scale, it is measured by comparing the applied load-debonding length curve. For the dynamic case, the similarity is measured by comparing the strain-time history at the gauge location and the change of the debonding length in relation to the maximum of the strain-time history.

Firstly, we discuss the similarity of the computational model and the experiment for the static case in the macroscopic scale. The comparison is made in Fig. 8 where the applied stress-displacement curves obtained from the two methods plotted. The curve obtained in the experiment shows that the matrix-matrix interface, ahead of

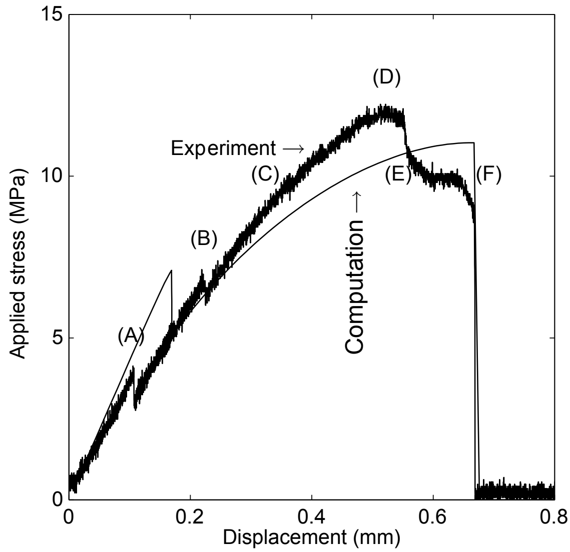

Fig. 8. The applied stress versus the displacement for the 1 mm bundled-fiber specimen: comparison between the experimental data and the numerical prediction

the notch, gradually fractures; meanwhile, in the computational model, the interface is designed to fracture at once. In addition, the experimental curve indicates that the bundled-fiber gradually fractures from point D until the final fracture, which occurs at point F. The nonlinearity of the curve, which indicates the propagation of the debonding, seems to start earlier in the model than that in the experiment.

For the dynamic case, the similarity between the model and experiment responses at the macroscopic scale is demonstrated by the strain-time history data at the measurement point (see Fig. 9). The evident depicted by Figs. 8 and 9 suggests

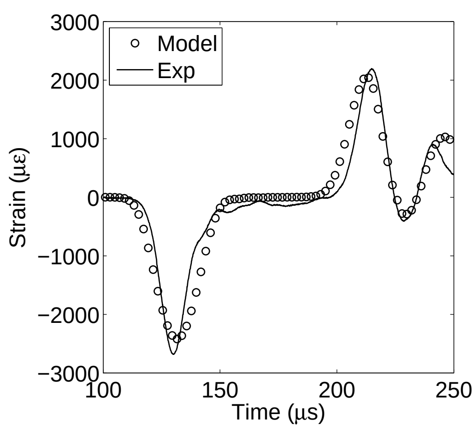

Fig. 9. Strain-time history at the gauge location for 1 mm bundled-fiber specimen [3]

that the model responses at the macroscopic scale seem to closely resemble to the experimentally observed responses.

Fig. 10 shows a comparison of the model prediction and the experimental data for the static case.

The model seems to provide better estimation for the 1 mm bundled-fiber diameter than for the 2 mm bundled-fiber diameter. However, it may be due to the nature of the data, which highly scatter for the latter case.

Fig. 11 shows a comparison for the dynamic case. Again, we see that the model reasonably estimates the propagation of the debonding.

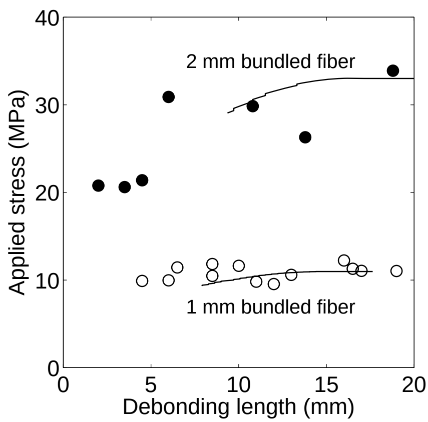

Fig. 10. Comparison of the experimental data and numerical prediction for the static case

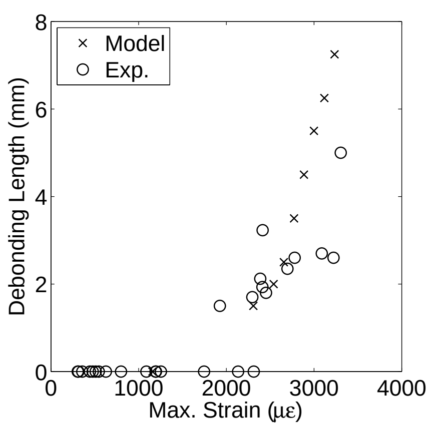

Fig. 11. Comparison of the experimental data ('∘') and numerical prediction ('×') for the stress-pulse case; the bundled fiber diameter is 1 mm; the maximum strains are those recorded by the two rear gauges (see Fig. 3)

The results of this study are concisely summarized in Table 1. The table shows that the dynamic strength is higher than the static strength by a factor of

3–4; meanwhile, the dynamic fracture energy is about twice higher than the static fracture energy.

The idea that the material strength and fracture energy is higher in the high loading rate is traditional and acceptable. For example, according to Zheng et al.[22], dynamic strength of concrete would increase by 30%–50% when the loading rate was varied from 1.5 to 3 1/s. In addition, Kalthoff and Wrinkler [23], as cited by Nishioka and Atluri [24], shown that the fracture toughness of Araldite B double-cantilever-beam specimen increased from 0.7 MPa·mm$^{1/2}$ at the static test to 1.4 MPa·mm$^{1/2}$ at the dynamic test with a crack speed of 300 m/s. Thus, these results in Table 1 seem to be reasonable.

Table 1.
The parameters of the cohesive zone model for the static and dynamic cases

Load Case	Parameter	Matrix-fiber interface	Matrix-matrix interface	Unit
Static	$T_{\mathbf{n}}^{c}$	15.0	21.0	MPa
	$T_{\mathbf{s}}^{c}$	15.0	–	MPa
	$G_{\mathbf{n}}^{c}$	1.0	1.0	MPa·mm
	$G_{\mathbf{s}}^{c}$	1.0	–	MPa·mm
Dynamic	$T_{\mathbf{n}}^{c}$	54.0	72.0	MPa
	$T_{\mathbf{s}}^{c}$	67.0	–	MPa
	$G_{\mathbf{n}}^{c}$	2.0	2.0	MPa·mm
	$G_{\mathbf{s}}^{c}$	2.0	–	MPa·mm

In regard to the debonding length prediction, the model was only capable estimating the debonding at a reasonable length, which was longer than 7.5 mm for the statically loaded case. However, when the load was dynamic, the smallest debonding was estimated at 2 mm length. These limitations were not affected by the mesh size as was indicated by a mesh sensitivity study.

4. Conclusions

Understanding the characteristics of the debonding of composite materials is important in order to safely use the materials for engineering applications. For the purpose, many methods have been proposed. Those methods are the micro-bond, the fiber pull-out, the fiber push-out, and the single-fiber fragmentation test methods. Each method has benefits and limitations. This article has discussed a method to test debonding subjected to the static load and the pulse-type load. The proposed method is experimentally verified, and the results indicates the proposed method, in conjunction with the cohesive zone model, is capable to quantify the debonding on those loading conditions. Clearly, the method has potential for use for the case of moderate rates of loading.

Manuscript received by Editorial Board, January 31, 2018;
final version, May 29, 2018.

References

[1] W.G. Roeseler, B. Sarh, and M. Kismarton: Composite structures: The first 100 years. In *Proceedings of 16th International Conference on Composite Materials*, Kyoto, Japan, July 9 2007.

[2] C. Shet and N. Chandra. Analysis of energy balance when using cohesive zone models to simulate fracture processes. *Transactions of the ASME: Journal of Engineering Materials and Technology*, 124:440–450, October 2002.

[3] F.E. Gunawan. Debonding strength of bundled glass fibers subjected to stress pulse loading. *Engineering Fracture Mechanics*, 78(16):2731–2745, Nov 2011. doi: 10.1016/j.engfracmech.2011.07.008.

[4] M.A. Minnicino and M.H. Santare. Modeling the progressive damage of the microdroplet test using contact surface with cohesive behavior. *Composites Science and Technology*, 72(16):2024–2031, 2012. doi: 10.1016/j.compscitech.2012.09.009.

[5] K.N. Anyfantis and N.G. Tsouvalis. Loading and fracture response of CFRP-to-steel adhesively bonded joints with thick adherents – Part II: Numerical simulation. *Composite Structures*, 96:858–868, 2013. doi: 10.1016/j.compstruct.2012.08.056.

[6] E. Nwankwo, A. Soleiman Fallah, and L.A. Louca. An investigation of interfacial stresses in adhesively-bonded single lap joints subject to transverse pulse loading. *Journal of Sound and Vibration*, 332(7):1843–1858, 2013. doi: 10.1016/j.jsv.2012.11.008.

[7] T. Schüller, W. Becker, and B. Lauke. Analytical and numerical calculation of the energy release rate for the micro bond test. *The Journal of Adhesion*, 70:33–56, 1999. doi: 10.1080/00218469908010486.

[8] L.P. Hann and D.E. Hirt. Simulating the microbond technique with macrodroplets. *Composites Science and Technology*, 54(4):423-430, 1995. doi: 10.1016/0266-3538(95)00080-1.

[9] B. Miller, P. Muri, and L. Rebenfeld. A microbond method for determination of the shear strength of a fiber/resin interface. *Composites Science and Technology*, 28(1):17–32, 1987. doi: 10.1016/0266-3538(87)90059-5.

[10] C.-H. Liu and J.A. Naim. Analytical and experimental methods for a fracture mechanics interpretation of the micro bond test including the effect of friction and thermal stresses. *International Journal of Adhesion and Adhesives*, 19(1):59–70, 1999. doi: 10.1016/S0143-7496(98)00057-8.

[11] J.-P. Favre and M.-C. Merienne. Characterization of fibre/resin bonding in composites using a pull-out test. *International Journal of Adhesion and Adhesives*, 1(6):311–316, 1981. doi: 10.1016/0143-7496(81)90025-7.

[12] J.-K. Kim, C. Baillie, and Y.-W. Mai. Interfacial debonding and fiber pull-out stresses. Part 1: Critical comparison of existing theories with experiments. *Journal of Materials Science*, 27(12):3143–3154, 1991. doi: 10.1007/BF01116004.

[13] J.K. Wells and P.W.R. Beaumont. Debonding and pull-out processes in fibrous composites. *Journal of Materials Science*, 20(4):1275–1284, 1985. doi: 10.1007/BF01026323.

[14] J.A. Nairn, C.-H. Liu, D.-A. Mendels, and S. Zhandarov. Fracture mechanics analysis of the single-fiber pull-out test and the micro bond test including the effect of friction and thermal stresses. In *Proceeding of 16th Annual Technology Conference of the American Society of Composites*, Blacksburg, VA, USA, 9–12 September, 2001.

[15] L.-M. Zhou, Y.-W. Mai, and L. Ye. Analyses of fiber push-out test based on the fracture mechanics approach. *Composites Engineering*, 5(10-11):1199–1219, 1995. doi: 10.1016/0961-9526(95)00053-P.

[16] G. Lin, P.H. Geubelle, and N.R. Sottos. Simulation of fiber debonding and frictional sliding in a model composite push-out test. *International Journal of Solids and Structures*, 38(46-47):8547–8562, 2001. doi: 10.1016/S0020-7683(01)00085-3.

[17] Z. Li, X. Bi, J. Lambros, and P.H. Geubelle. Dynamic fiber debonding and frictional push-out in model composites systems: experimental observations. *Experimental Mechanics*, 42(4):417–425, 2002. doi: 10.1007/BF02412147.

[18] X. Bi, Z. Li, P.H. Geubelle, and J. Lambros. Dynamic fiber debonding and frictional push-out in model composite systems: numerical simulations. *Mechanics of Materials*, 34(7):433–446, 2002. doi: 10.1016/S0167-6636(02)00141-2.

[19] Abaqus. *ABAQUS Analysis User's Manual Version 6.8*, 2008.

[20] P.H. Geubelle and J. Baylor. The impact-induced delamination of laminated composites: A 2D simulation. *Composites, Part B: Engineering*, 29(5):589–602, 1998. doi: 10.1016/S1359-8368(98)00013-4.

[21] P.P. Camanho and C.G. Davila. Mixed-mode decohesion finite elements for the simulation of delamination in composite materials. Technical Report NASA/TM-2002-211737, NASA Langley Research Center, Hampton, VA, USA, June 2002.

[22] D. Zheng and Q. Li. Micromechanics model for static and dynamic strength of concrete under confinement. *Frontiers of Architecture and Civil Engineering in China*, 24):329–335, 2008. doi: 10.1007/s11709-008-0044-4.

[23] J.F. Kalthoff, J. Beinert, and S. Wrinkler. Measurement of dynamic stress intensity factors for fast running and arresting cracks in double-cantilever-beam specimens. In *Fast Fracture and Crack Arrest*, Proceedings of Symposium, Chicago, 28-30 June 1976. ASTM STP 627, pages 161–176, 1977. doi: 10.1520/STP27387S.

[24] T. Nishioka and S.N. Atluri. A numerical study of the use of path independent integrals in elasto-dynamic crack propagation. *Engineering Fracture Mechanics*, 18(1):23–33, 1983. doi: 10.1016/0013-7944(83)90092-9.

[25] S. Feih, K. Wonsyld, D. Minzari, P. Westermann, and H. Lilholt. Testing procedure for the single fiber fragmentation test. Technical Report Riso-R-1483, Riso National Laboratory, Roskilde, Denmark, December 2004.

[26] A. Awal, G. Cescutti, S.B. Ghosh, and J. Müssig. Interfacial studies of natural fibre/polypropylene composites using single fibre fragmentation test (SFFT). *Composites Part A: Applied Science and Manufacturing*, 42(1):50–56, 2011. doi: 10.1016/j.compositesa.2010.10.007.

[27] D. Tripathi and F.R Jones. Single fibre fragmentation test for assessing adhesion in fibre reinforced composites. *Journal of Materials Science*, 33(1):1–16, 1998. doi: 10.1023/A:1004351606897.